Mathematical Biosciences and Engineering

http://www.aimspress.com/journal/mbe

MBE, 21(4): 5047–5067.
DOI: 10.3934/mbe.2024223
Received: 11 December 2023
Revised: 09 February 2024
Accepted: 26 February 2024
Published: 04 March 2024

Research article

Sparse-view X-ray CT based on a box-constrained nonlinear weighted anisotropic TV regularization

Huiying Li and Yizhuang Song*

School of Mathematics and Statistics, Shandong Normal University, Jinan 250014, China

* **Correspondence:** Email: ysong@sdnu.edu.cn.

Abstract: Sparse-view computed tomography (CT) is an important way to reduce the negative effect of radiation exposure in medical imaging by skipping some X-ray projections. However, due to violating the Nyquist/Shannon sampling criterion, there are severe streaking artifacts in the reconstructed CT images that could mislead diagnosis. Noting the ill-posedness nature of the corresponding inverse problem in a sparse-view CT, minimizing an energy functional composed by an image fidelity term together with properly chosen regularization terms is widely used to reconstruct a medical meaningful attenuation image. In this paper, we propose a regularization, called the box-constrained nonlinear weighted anisotropic total variation (box-constrained NWATV), and minimize the regularization term accompanying the least square fitting using an alternative direction method of multipliers (ADMM) type method. The proposed method is validated through the Shepp-Logan phantom model, alongisde the actual walnut X-ray projections provided by Finnish Inverse Problems Society and the human lung images. The experimental results show that the reconstruction speed of the proposed method is significantly accelerated compared to the existing L_1/L_2 regularization method. Precisely, the central processing unit (CPU) time is reduced more than 8 times.

Keywords: sparse-view CT; computed tomography; box-constrained anisotropic TV; regularization; inverse problems

1. Introduction

In clinical applications, X-ray computed tomography (CT) aims to visualize the internal structure of the human body by reconstructing the tissues' attenuation coefficients μ to X-rays. Depending on diverse X-ray sources, there are parallel beam, fan beam, and cone beam CTs [1–4]. In this paper, for ease of explanation, we focus on image reconstructions in parallel beam CT, even though the proposed method can be used in other fan beam and cone beam CTs. In a parallel beam CT, parallel X-ray beams in different directions are transmitted through the patient, who lies between the X-ray sources and the

detectors (see Figure 1). The corresponding attenuated X-ray intensities are measured through the detectors. The inverse problem of a parallel beam CT is to reconstruct the attenuation coefficient from the received attenuated X-ray intensities. Given the perfect measured data, the reconstruction methods include filtered back-projection, the algebraic reconstruction technique (ART) [1], and so on. Due to the advantages of speed, accuracy, and excellence with bones and lungs for nondestructive testing, X-ray CT is widely used in medical imaging to aid doctors in diagnosing diseases [1].

Nevertheless, exposure of the patients to the environment of radiation increases the risk of many diseases such as leukemia, cancer, etc [5]. Low dose CT is an effective way to reduce such a risk. There are generally three methods of low dose CT. The first is to reduce the tube voltage/currents, the second is the limited angle CT reconstruction, and the third is the sparse-view CT reconstruction. For the first method, to obtain a meaningful CT image, we need an efficient denoising algorithm [6]. For the second method, visible singularities, invisible singularities, and artifacts exist [1]. For the third method, since it violates the Nyquist/Shannon sampling criterion, strong streaking artifacts will occur [7]. In this paper, we focus on removing the streaking artifacts in the sparse-view CT reconstruction. To this end, we need to develop efficient ways to deal with the ill-posedness caused by the projection downsamplings [1].

To deal with the ill-posedness, the data-driven and model-driven methods exist. The data-driven method includes the usage of a convolutional neural network (CNN) [8], U-Net [9], and the GoogLeNet [10]. However, as pointed out in [11], there should be more evidence of such methods being used in clinical applications. For the sparse-view CT, it is also very difficult to provide enough labeled data, since we cannot produce the data with full projections without enough doses. Hence, the model-driven method is still quite necessary.

For the model-driven method, note that the algebraic method [12] has the flexibility of incorporating the a-priori information of μ. It is widely used in a sparse-view CT. To be precise, the reconstruction of μ is recast into a minimization problem of an energy functional constructed by a (weighted) least square fitting and a regularization.

Noting the piecewise constant structure of medical images, its gradient can be considered sparse. The study performed in [13] proposed the total variation (TV) regularization method in sparse-view CT. However, it is well known that TV will introduce new blocky/staircasing artifacts [14]. The study performed in [15] proposed the anisotropic TV regularization method, that could produce distortions along axes. To handle such problems, many variations of TV regularization have been proposed in the last two decades. The study performed in [16] proposed an edge-preserving TV regularizer which used the $e^{-|\nabla\mu|^2/\sigma^2}$ as the edge detector, where σ was a prescribed parameter that represented the amount of smoothing. Later, [17] proposed a similar discretized version to [16]. The similar methods can be found in [18, 19]. Nevertheless, the ability of removing the streaking artifact and edge-preserving can be further improved due to the fact that the amount of regularization near the edges and away from that does not differ much since $e^{-|\nabla\mu|^2/\sigma^2} \in [0, 1]$. The study performed in [20] proposed the total generalized variation (TGV) regularizer, which used the second order derivative of the unknown μ. While this method can avoid the blocky artifacts, it assumes the piecewise linear structure of the image. It is well known that the piecewise constant is commonly used for a medical image. The study performed in [21] proposed a directional TV regularizer in which a directional derivative was considered, rather than just using $\nabla\mu$. However, different weights can employed in different directions to improve the performance of this method. The study performed in [22] proposed the $L^p(0 < p < 1)$ regularization method. However, the images heavily relied on the parameter p.

L_1/L_2 is a recently proposed regularization technique [23]. This method is based on updating the regularization parameter in each iteration. However, the updating parameter is not region-dependent, that is, in each iteration, the minimization problem is isotropic. The study performed in [24] proposed a nonlinear weighted anisotropic TV (NWATV) regularization method and used it in electrical impedance tomography, which is a low resolution imaging modality. In this paper, a box-constrained NWATV method was used in sparse-view CT, which produced a significantly improved reconstruction compared with directly using NWATV and box-constrained L_1/L_2 methods. Precisely, across the internal edges where $\nabla\mu \to \infty$, we set the regularization to be small to preserve the edge, while near the smooth region, we set a normal regularization to make the ill-posed problem better posed. We found a significant convergence behavior of the iteration process with the box constraint (set the reconstruction value lies in a proper interval). We validated the proposed algorithm using the Shepp-Logan phantom, the walnut X-ray data provided by Finnish Inverse Problems Society (http://fips.fi/dataset.php), and the clinical lung image provided by The Cancer Imaging Archive (TCIA: https://www.cancerimagingarchive.net/collection/lungct-diagnosis/).

The rest of the paper is organized as follows. In Section 2, we provide a brief introduction of the parallel beam CT. In Section 3, we introduce the proposed box-constrained nonlinear weighted anisotropic TV regularization and provide an iterative reconstruction algorithm. In Section 4, we validate the performance of the proposed regularization method using the Shepp-Logan phantom, the actual walnut CT experiment data, and the clinical lung image. In Section 5, we discuss the rules of the choice of regularization parameters. In Section 6, we conclude the paper and provide some future research topics.

2. Preliminaries of parallel beam CT

In parallel beam CT, we restrict our explanations to the two-dimensional space because the parallel beam always lies in a plane, and each time, the X-ray can only pass through a slice of the object. Let $\Omega \subset \mathbb{R}^2$ represent a bounded region of the imaging object. Denote μ as the attenuation coefficient of Ω, which is generally a piecewise constant function in medical imaging. In parallel beam CT, an incident X-ray beam along the direct lines $L_{\theta,s} := \{\mathbf{x} \in \mathbb{R}^2 \ : \ \Theta \cdot \mathbf{x} = s\}$ passes through the object, which lies between the X-ray sources and the detectors (see Figure 1). Here, $s \in \mathbb{R}$ denotes the signed distance of $L_{\theta,s}$ to the original point $O(0,0)$ and $\Theta = (\cos\theta, \sin\theta)$, with $\theta \in [0, \pi)$ denoting the angle of a directly line l and x-axis, where l is perpendicular to $L_{\theta,s}$. We assume that the incident X-ray intensity is I^0. For a fixed θ and s, the attenuated X-ray intensity $I(\theta, s)$ can be measured through the detector. The relation between the measured $I(\theta, s)$ and the unknown μ is described by the Lambert-Beer law [1, 2]:

$$I(\theta, s) = I^0 \exp\{-\mathcal{R}_\theta[f](s)\},$$

where $\mathcal{R}_\theta[f](s)$ is the Radon transform [25] of f, which is defined as follows:

$$\mathcal{R}_\theta[f](s) = \int_{L_{\theta,s}} \mu(\mathbf{x}) d\ell_{\mathbf{x}}$$

with $d\ell_{\mathbf{x}}$ denoting the length element.

In medical imaging, we assume that a parallel beam contains J X-rays, and hence J-detectors are employed to detect the corresponding attenuated X-rays. We assume that the J X-rays are equidistantly

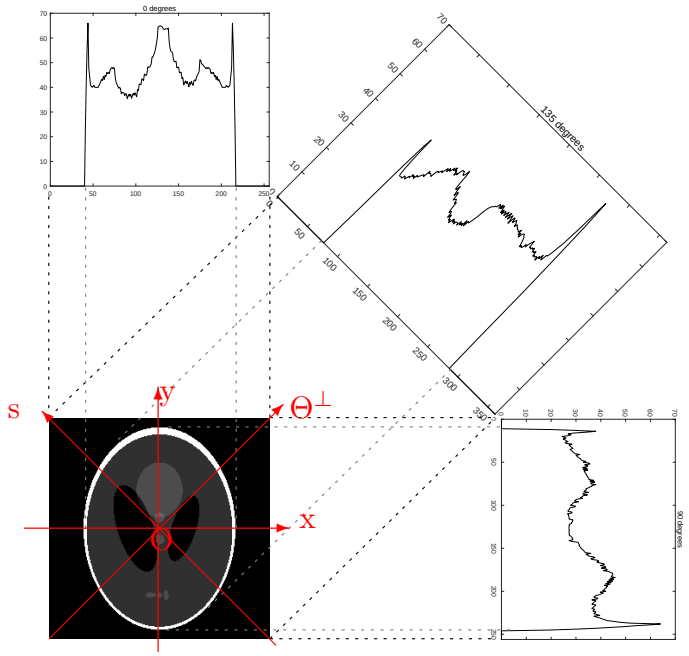

Figure 1. Schematic diagram of a parallel X-ray beam CT system.

distributed. To be precise, we assume that the signed distances of the X-rays to the original point lie in $[\underline{s}, \bar{s}]$, and the signed distance of the j-th ($j \in \{1, 2, \cdots, J\}$) X-ray to the original point is $s_j = \underline{s} + (j-1)(\bar{s} - \underline{s})/(J-1)$. Moreover, we utilize K angles $\theta_k = (k-1)\pi/K$ for $1 \le k \le K$ and $k \in \mathbb{Z}_+$. Then, through the detectors $M := JK$, projection datum $I(\theta_k, s_j)$ ($1 \le j \le J$ and $1 \le k \le K$) can be measured.

For ease of explanation, we denote $y_m = \ln \frac{I^0}{I(\theta_k, s_j)}$ for $m = J(k-1) + j$. Then, we have the following:

$$y_m = \int_{L_{\theta_k, s_j}} \mu(\mathbf{x}) d\ell_{\mathbf{x}} \tag{2.1}$$

for $1 \le m \le M$. Suppose the field of view (FOV) is the square, and FOV $= [a, b] \times [a, b]$ which satisfies $\Omega \subset$ FOV. We discretize FOV to be $N \times N$ pixels P_{qt} ($1 \le q, t \le N$). Then, from Eq (2.1), the reconstruction of μ can be recast to solve the following linear system:

$$\mathbf{y} = A\mathbf{u}. \tag{2.2}$$

Here, $A = (a_{mp})$ is an $M \times n$ matrix for $n = N^2$, $\mathbf{y} = (y_m)$ is an $M \times 1$ vector, and $\mathbf{u} = (u_p)$ is an $n \times 1$ vector. To be precise, a_{mp} is the length of the projection line which lies in the pixel P_{qt}, i.e., $a_{mp} = |L_{\theta_k, s_j} \cap P_{qt}|$ for $p = N(t-1) + q$, $u_p = \mu(q, t)$ and y_m is defined in Eq (2.1).

3. Nonlinear weighted anisotropic TV regularization with box constraint

Note that for the sparse-view CT, we generally have $M \ll n$; hence, to solve Eq (2.2), we reformulate it to the following least squares problem:

$$\mathbf{u}^* = \arg\min_{\mathbf{u}} \|A\mathbf{u} - \mathbf{y}\|_{\ell_2}^2, \tag{3.1}$$

where $\|\cdot\|_{\ell_2}$ denotes the standard Euclidean norm in $\mathbb{R}^M$. Since A^TA is ill-conditioned, where $\cdot^T$ represents the transpose of $\cdot$, we approximate Eq (3.1) by the following well-conditioned problem:

$$\mathbf{u}^* = \arg\min_{\mathbf{u}} \left\{ \frac{1}{2}\|A\mathbf{u} - \mathbf{y}\|_{\ell_2}^2 + \lambda \text{Reg}(\mathbf{u}) \right\}. \tag{3.2}$$

The first term on the right-hand side of Eq (3.2) is the data fidelity term, the second term Reg($\mathbf{u}$) is the regularization term, and λ is the regularization parameter that balances the fidelity and the regularization terms. Precisely, instead of seeking the solution in the space ℓ_2, where there may be infinitely many solutions, we seek the solution in its subspace, which is characterized by Reg($\mathbf{u}$).

Since the edge of the internal structure is a key feature in medical imaging, the choice of the term Reg($\mathbf{u}$) should obey the following rule:

- Near the local edges of μ or $\mathbf{u}$ where $|\nabla\mu| \approx \infty$, do as little regularization as possible to preserve the edges.
- Perform a normal regularization when μ is smooth (i.e., $|\nabla\mu|$ is small to make Eq (3.2) well-posed).
- The range of the reconstructed $\mathbf{u}$ coincides with the range of its true value.

Combining the above three considerations, we define Reg($\mathbf{u}$) as follows:

$$\text{Reg}(\mathbf{u}) = \|\mathbf{p} \cdot \mathcal{D}\mathbf{u}\|_{\ell_1} + \frac{\gamma}{\lambda}\Pi_{[c_1,c_2]}(\mathbf{u}), \tag{3.3}$$

where γ is the indicator of using box constraint, that is, $\gamma = 1$ if the box constraint is used, while $\gamma = 0$ if no box constraint is employed. Here, $\mathbf{p} = \left(\omega(\mathcal{D}_x\mathbf{u}); \omega(\mathcal{D}_y\mathbf{u})\right) \in \mathbb{R}^{2n}$, $\mathcal{D}\mathbf{u} = (\mathcal{D}_x\mathbf{u}; \mathcal{D}_y\mathbf{u}) \in \mathbb{R}^{2n}$, where $\mathcal{D}_x$, $\mathcal{D}_y \in \mathbb{R}^{n\times n}$ are the first-order difference operators along the x and y directions, respectively, $\omega(\cdot) = \frac{1}{|\cdot|^2+\beta}$ with $\beta > 0$ a small positive number to avoid zero being the denominator; $\Pi_{[c_1,c_2]}(\mathbf{u})$ is an indicator function, which equals to 0 if for all $i \in \{1, 2, \cdots, n\}$, where $\mathbf{u}[i] \in [c_1, c_2]$, and equals to $+\infty$ otherwise. Note that $\Pi_{[c_1,c_2]}$ is capable of enforcing $\mathbf{u}$ into the range of the actual attenuation coefficient.

The augmented Lagrangian functional of Eq (3.2), together with Eq (3.3), can be expressed as follows:

$$\begin{aligned}\mathcal{L}(\mathbf{u}, \mathbf{d}, \mathbf{p}, \mathbf{v}; \mathbf{b}, \mathbf{e}) = &\frac{1}{2}\|A\mathbf{u} - \mathbf{y}\|_{\ell_2}^2 + \lambda\|\mathbf{p} \cdot \mathbf{d}\|_{\ell_1} + < \mathbf{b}, \mathcal{D}\mathbf{u} - \mathbf{d} > \\ &+ \frac{\rho}{2}\|\mathcal{D}\mathbf{u} - \mathbf{d}\|_{\ell_2}^2 + \Pi_{[c_1,c_2]}(\mathbf{v}) + < \mathbf{e}, \mathbf{u} - \mathbf{v} > + \frac{\alpha}{2}\|\mathbf{u} - \mathbf{v}\|_{\ell_2}^2,\end{aligned} \tag{3.4}$$

where $\mathbf{d}$, $\mathbf{v}$ are the auxiliary variables, $\mathbf{b}$, $\mathbf{e}$ are the Lagrangian multipliers, and ρ, α are the scalar penalty parameters.

To minimize Eq (3.4), we use the alternating direction method of multipliers (ADMM) [26]. To be precise, for an initial guess $(\mathbf{d}^{(0)}, \mathbf{p}^{(0)}, \mathbf{v}^{(0)}, \mathbf{b}^{(0)}, \mathbf{e}^{(0)})$, $\mathbf{u}$ is iteratively updated via the following scheme:

$$\mathbf{u}^{(k+1)} = \arg\min_{\mathbf{u}} \mathcal{L}(\mathbf{u}, \mathbf{d}^{(k)}, \mathbf{p}^{(k)}, \mathbf{v}^{(k)}; \mathbf{b}^{(k)}, \mathbf{e}^{(k)}); \tag{3.5a}$$

$$\mathbf{d}^{(k+1)} = \arg\min_{\mathbf{d}} \mathcal{L}(\mathbf{u}^{(k+1)}, \mathbf{d}, \mathbf{p}^{(k)}, \mathbf{v}^{(k)}; \mathbf{b}^{(k)}, \mathbf{e}^{(k)}); \tag{3.5b}$$

$$\mathbf{p}^{(k+1)} = \left(\omega(\mathcal{D}_x\mathbf{u}^{(k+1)}); \omega(\mathcal{D}_y\mathbf{u}^{(k+1)})\right); \tag{3.5c}$$

$$\mathbf{b}^{(k+1)} = \mathbf{b}^{(k)} + \rho\left(\mathcal{D}\mathbf{u}^{(k+1)} - \mathbf{d}^{(k+1)}\right); \tag{3.5d}$$

$$\mathbf{v}^{(k+1)} = \min\{\max\{\mathbf{u}^{(k+1)} + \frac{1}{\alpha}\mathbf{e}^{(k)}, c_1\}, c_2\}; \tag{3.5e}$$

$$\mathbf{e}^{(k+1)} = \mathbf{e}^{(k)} + \alpha(\mathbf{u}^{(k+1)} - \mathbf{v}^{(k+1)}). \tag{3.5f}$$

For Eq (3.5a) and Eq (3.5b), the minimizers have the following closed form:

$$\begin{aligned}\mathbf{u}^{(k+1)} = &\left[A^TA + \rho\mathcal{D}^T\mathcal{D} + \alpha\mathcal{I}\right]^{-1} \\ &\left[A^T\mathbf{y} + \rho\mathcal{D}^T\mathbf{d}^{(k)} - \mathcal{D}^T\mathbf{b}^{(k)} - \mathbf{e}^{(k)} + \alpha\mathbf{v}^{(k)}\right],\end{aligned} \tag{3.6}$$

and

$$\mathbf{d}^{(k+1)}[i] = h_{\frac{\lambda|\mathbf{p}^{(k)}[i]|}{\rho}}\left(\mathcal{D}\mathbf{u}^{(k+1)}[i] + \frac{1}{\rho}\mathbf{b}^{(k)}[i]\right). \tag{3.7}$$

Here, $\mathcal{I}$ is an $n \times n$ identity matrix; $\mathbf{b}^{(k)}[i]$, $\mathbf{p}^{(k)}[i]$, $\mathbf{u}^{(k+1)}[i]$, and $\mathbf{d}^{(k+1)}[i]$ are the i-th element of $\mathbf{b}^{(k)}$, $\mathbf{p}^{(k)}$, $\mathbf{u}^{(k+1)}$, and $\mathbf{d}^{(k+1)}$, respectively, and $h_g(\cdot)$ represents the soft threshold formula, which is defined as follows [27]:

$$h_g(\cdot) = \begin{cases} \cdot - g\text{sgn}(\cdot), & \text{if } |\cdot| > g \\ 0, & \text{otherwise,} \end{cases}$$

where sgn is the sign function.

We end this section by summarizing the aforementioned process as the reconstruction algorithm in the form of the pseudocode shown in Algorithm 1.

Algorithm 1 The box-constrained NWATV method

Require: Projection matrix A, observed data $\mathbf{y}$, and a bound $[c_1, c_2]$ for the original image.
Parameters: $\rho, \lambda, \beta, \alpha, \in \mathbb{R}^+$, a tolerance $\bar{\epsilon}$ and the maximum iteration number kMax$\in \mathbb{Z}^+$.
Ensure: the reconstructed image $\mathbf{u}$

Initialize: $\mathbf{d}^{(0)} = \mathbf{0}, \mathbf{p}^{(0)} = (\frac{1}{\beta})\mathbf{1}, \mathbf{b}^{(0)} = \mathbf{0}, \mathbf{v}^{(0)} = \mathbf{0}, \mathbf{e}^{(0)} = \mathbf{0}, \mathbf{u}^{(0)} = \mathbf{0}$.
for k=0:kmax-1 **do**
  Update $\mathbf{u}^{(k+1)}$ using (3.6).
  Update $\mathbf{d}^{(k+1)}$ using (3.7).
  Update $\mathbf{p}^{(k+1)}$ using (3.5c).
  Update $\mathbf{b}^{(k+1)}$ using (3.5d).
  Update $\mathbf{v}^{(k+1)}$ using (3.5e).
  Update $\mathbf{e}^{(k+1)}$ using (3.5f).
  if $\|\mathbf{u}^{(k+1)} - \mathbf{u}^{(k)}\|_{\ell_2} < \bar{\epsilon}$ **then**
    break
  end if
end for

4. Experiments

In this section, to validate the advantages of the proposed regularization, we perform experiments using the Shepp-Logan numerical model, the walnut actual CT model provided by Finnish Inverse

Problems Society (http://fips.fi/dataset.php), and the clinical CT image provided by The Cancer Imaging Archive (https://www.cancerimagingarchive.net/collection/lungct-diagnosis/). Additionally, the walnut CT data is provided in ZENODO (https://zenodo.org/record/1254206). The experimental models are shown in Figure 2 .

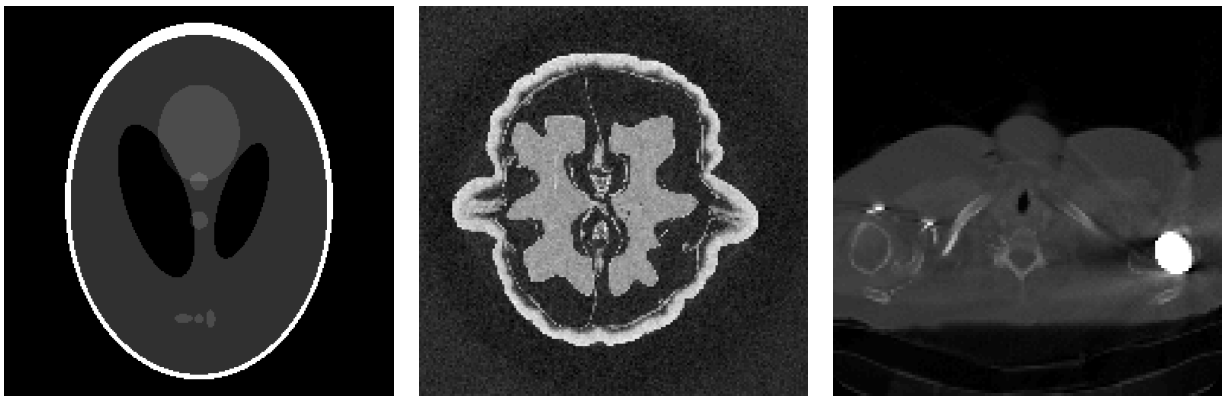

(a) Shepp-Logan model (b) Walnut model (c) Clinical lung image

Figure 2. Experimental models we used. (a) is the Shepp-Logan phantom model in numerical experiment, (b) shows the walnut model in actual CT experiment which is obtained in Finnish Inverse Problems Society (FINNISH), and (c) is a clinical lung image provided by the Cancer Image Archive (TCIA).

4.1. Experiment setup

To show the advantages of the proposed regularization, we compare the reconstructions of the most recently proposed gradient-based L_1/L_2 [23] with box constraint and the nonlinear weighted anisotropic TV regularization [24] with box constraint. To compare the performance of the reconstructions, we compute the relative errors (including the L^2 relative errors RE(k) and the H^1 relative errors $\widetilde{\text{RE}}(k)$) and mean square errors MSE(k) for the k-th step as follows:

$$\text{RE}(k) = \frac{\|\mathbf{u}^{(k)} - \mathbf{u}_0\|_{\ell_2}}{\|\mathbf{u}_0\|_{\ell_2}},$$

$$\widetilde{\text{RE}}(k) = \frac{\sqrt{\|\mathbf{u}^{(k)} - \mathbf{u}_0\|_{\ell_2}^2 + \|\mathcal{D}(\mathbf{u}^{(k)} - \mathbf{u}_0)\|_{\ell_2}^2}}{\sqrt{\|\mathbf{u}_0\|_{\ell_2}^2 + \|\mathcal{D}\mathbf{u}_0\|_{\ell_2}^2}},$$

and

$$\text{MSE}(k) = \frac{\|\mathbf{u}^{(k)} - \mathbf{u}_0\|_{\ell_2}^2}{n}.$$

Here, $\mathbf{u}^{(k)}$ represents the result of the reconstruction at the k-th step. In the Shepp-Logan phantom, $\mathbf{u}_0$ represents the ground truth image; in the walnut experiment, it represents the CT image reconstructed using full projections and the filtered back-projection (FBP) method, since we do not know the ground

truth image in the actual experiment; in the lung image, it represents the actual image from TCIA. Figure 2(a)–(c) illustrate $\mathbf{u}_0$ of the Shepp-Logan phantom, the walnut, and the lung experiments.

Besides, we also compare the peak signal-to-noise ratio PSNR(k) and the structural similarity index SSIM(k) [28] for the k-th step, which is defined as follows:

$$\mathrm{PSNR}(k) = 10\log_{10}\frac{\max(\mathbf{u}^{(k)} \odot \mathbf{u}^{(k)})}{\mathrm{MSE}(k)},$$

and

$$\mathrm{SSIM}(k) = \frac{(2\mu_k\mu_0 + C_1)(2\sigma_{k0} + C_2)}{(\mu_k^2 + \mu_0^2 + C_1)(\sigma_k^2 + \sigma_0^2 + C_2)},$$

where $\cdot \odot \cdot$ represents the componentwise multiplication, μ_k and σ_k represent the local mean and the local standard deviation of $\mathbf{u}^k$, respectively, and μ_0 and σ_0 represent the local mean and the local standard deviation of $\mathbf{u}_0$, respectively; moreover, σ_{k0} denotes the cross-covariance of $\mathbf{u}^{(k)}$ and $\mathbf{u}_0$, and $C_1 = 10^{-4}, C_2 = 9 \times 10^{-4}$ are set to be the default values in the Matlab build-in function "ssim".

In the numerical experiment, we set the size of the reconstructed images to be 256×256 pixels and set the number of detectors to be $J = 362$. In the reconstruction of the actual walnut experiment, the size of the reconstructed images is set to be 164×164, and the number of detectors is also 164. In the lung image, we use the first image of patient R_172 in the dataset. The original size is 512×512, though we evenly sample to get the ground truth image of 128×128. The number of detectors is set to be 181. Using the Radon transform, we obtain the projection data corresponding to the lung image. To solve Eq (3.6), we use the generalized minimal residual algorithm (GMRES) [29] to accelerate the computation.

The reconstructions are carried out using Matlab 2018a (The MathWorks, Inc., Natick, MA, USA) on a workstation with 1.60 GHz Inter (R) Core (TM) i5-8250U CPU, 8.00 GB memory, Windows 10 operating system. Additionally, we use the MATLAB package AIR Tools II to simulate the *parallel beam* for the CT scanning [30].

4.2. Numerical experiment results

Under box constraints, we compare the results of L_1/L_2 method and nonlinear weighted TV regularization. In all experiments, we set the maximum number of external and internal iterations in the box-constrained L_1/L_2 to be 300 and 5, respectively. For fair comparisons, the ranges of other parameters are set according to [23] to minimize the L^2 relative error (RE) and to obtain the best performance. The number of iterations in NWATV(without box constraint) and the box-constrained NWATV regularization is set to be 300. We set the candidate set of parameters to be $\lambda \in \{0.002, 0.004, 0.006, 0.008, 0.01\}$, $\rho \in \{20, 40, 60, 200, 400, 600\}$, and $\alpha \in \{5, 20, 40, 60\}$. The selection of parameters has been carefully optimized to achieve a balance between minimizing the RE and optimizing the visual effects. Henceforth, in the figures and tables, we use L_1/L_2-box and NWATV-box as the abbreviations of the box-constrained L_1/L_2 and the box-constrained NWATV, respectively.

First, we consider the effect of box constraint for the NWATV regularization. We consider a parallel beam CT reconstruction with 31 angles uniformly taken from 0° to 150°, and the noise level is 0.5%. The box constraint is [0,1]. Therefore, the sample size is set to be 362×31. We do our best to choose the parameters such that RE attains the minimum value. Precisely, we choose $\rho = 20$, $\lambda = 0.002$, $\alpha =$

5 in the box-constrained NWATV, and $\rho = 20$, $\lambda = 0.004$ in NWATV. The reconstruction images are shown in Figure 3, and the corresponding relative errors (RE and $\widetilde{\text{RE}}$), mean square errors (MSE), peak signal-to-noise rations (PSNR), SSIM values, and the CPU times are shown in Table 1.

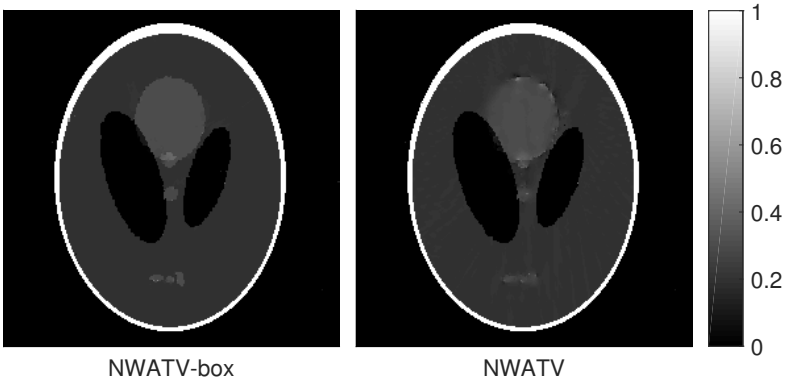

Figure 3. Effect of box constraint in NWATV reconstruction. The grayscale window is [0,1]. Left: Reconstruction result under box constraint. Right: Reconstruction result without box constraint.

Table 1. Numerical results of the Logan-Shepp model using the NWATV reconstruction with and without box constraint.

	RE	$\widetilde{\text{RE}}$	MSE	PSNR	SSIM	CPU time (s)
NWATV-box	0.042	0.077	1.0826×10^{-4}	39.670	0.987	264.279
NWATV	0.046	0.079	1.3087×10^{-4}	40.976	0.947	507.000

The results show that with a short reconstruction time, the box-constrained NWATV regularization can perform better than that without the box constraint. In Figure 4, we illustrate the evolutions of RE(k) and SSIM(k) with k, the iteration step. The figure clearly shows that the box constraint improves the convergence behavior of the NWATV method.

Next, we show that the proposed regularization can reconstruct a satisfied image using different sampling angles and is robust against the Gaussian random noise. We evenly take 90, 60, and 30 angles for comparisons from 0° to 179°. For each case, we add different Gaussian random noises with the levels 0.5%, 1%, 1.5%, and 2%. The box constraint is set to be [0,1].

We list the specific parameters selected in Table 2. The corresponding reconstruction results are shown in Figures 5–7. We show the values of the corresponding numerical results in Table 3.

As we can see from the reconstructions, the box-constrained NWATV can achieve numerical results similar to that of the box-constrained L_1/L_2 method at each sampling size. However, the CPU time is reduced at least 8 times. Taking visual effects into account, in the case of small angles (362×30), as the noise level increases, the box-constrained NWATV has more advantages than the box-constrained L_1/L_2 in noise removal and detail recovery.

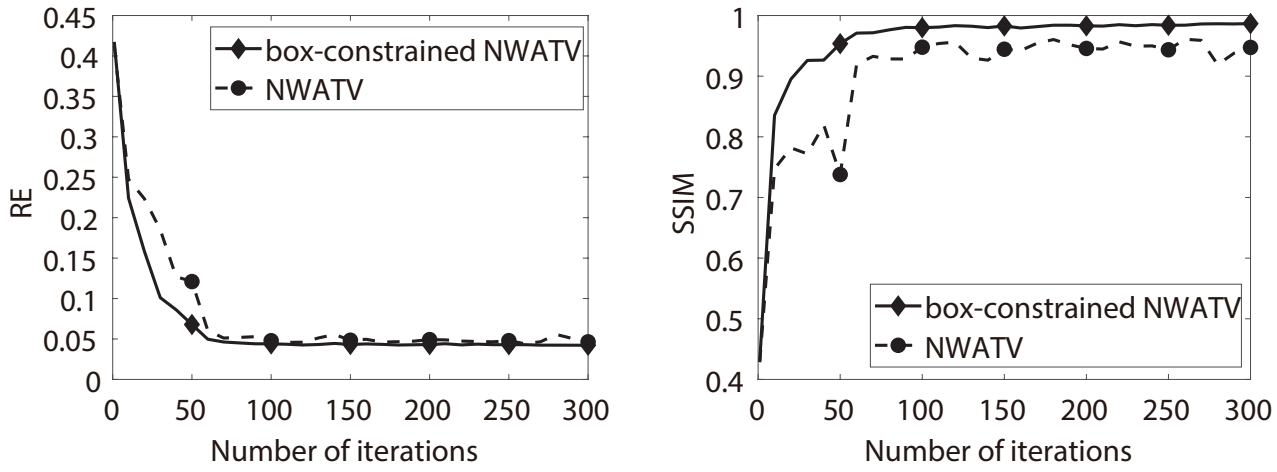

Figure 4. The effect of box constraint on the convergence of the iteration scheme of NWATV. The left is the RE and the right is the SSIM.

4.3. Walnut CT experiment and human lung experiment

First, in this section, we validate the performance of the proposed regularization method using the walnut data from the experimental datasets [31], which includes its complete projection matrix $\bar{A} \in \mathbb{R}^{19680\times 26896}$ and the projection data $\bar{\mathbf{y}} \in \mathbb{R}^{164\times 120}$ (3° per projection). We evenly subsample 50 angles from 0° to 149° by employing the first 50 projections. Then, the corresponding projection matrix A is also subsampled such that $A \in \mathbb{R}^{8200\times 26896}$. We use a high-resolution filtered back-projection reconstruction [31], and then evenly sample the obtained image to obtain the reference image $\mathbf{u}_0$, which is shown in Figure 2(b). From the reference image, we can estimate the box constraint is [0,0.6]. Considering the magnitudes of A^TA and $\mathcal{D}^T\mathcal{D}$, the parameters we take here are listed as follows: $\rho = 0.4$, $\lambda = 0.0001$, and $\alpha = 5$. For the parameters in the box-constrained L_1/L_2, we balance noise removal and detail recovery, choosing a set of parameters with the best visual effects. The results are shown in Figure 8, and the values of the corresponding numerical results are shown in Table 4. The arrows in Figure 8 depict that the box-constrained NWATV method perfoms better than the box-constrained L_1/L_2 in edges and details preserving.

Finally, we discuss the application of the two methods to clinical data [32]. We uniformly sample the image of 512×512 to obtain the image of 128×128, which is shown in Figure 2(c), and we represent it as the column vector $\mathbf{u}_0 \in \mathbb{R}^{128^2}$. We consider parallel beam scanning and set the sampling sizes as 181×60 and 181×30 to obtain the projection matrix A. The projection is $\mathbf{y} = A\mathbf{u}_0$. Since there is already noise in the lung image, we do not need to add additional noise any more. The box constraint is taken as [0,0.06]. In the experiment of box-constrained NWATV, we set the parameters as $\lambda = 0.001$, $\rho = 3 \times 10^{-9}$, and $\alpha = 0.01$ for both the 30 and 60 degrees projections. As in the box-constrained L_1/L_2, we balance noise removal and detail recovery, choosing a set of parameters to make the reconstructed image have the best visual effect. The results are shown in Figure 9, and the corresponding numerical results are shown in Table 5.

For further comparison, we also illustrate profiles of the reconstructed walnut and human lung images along the dash lines shown in Figure 10. From the profiles, it's clear that the proposed model

Table 2. Choices of parameters ρ, λ and α.

sampling size	noise level (%)	ρ	λ	α
362×90	0.5	20	0.004	60
	1	200	0.01	5
	1.5	400	0.01	5
	2	600	0.01	40
362×60	0.5	20	0.004	60
	1	200	0.01	5
	1.5	400	0.01	5
	2	600	0.01	5
362×30	0.5	60	0.002	60
	1	200	0.002	5
	1.5	400	0.002	20
	2	600	0.002	20

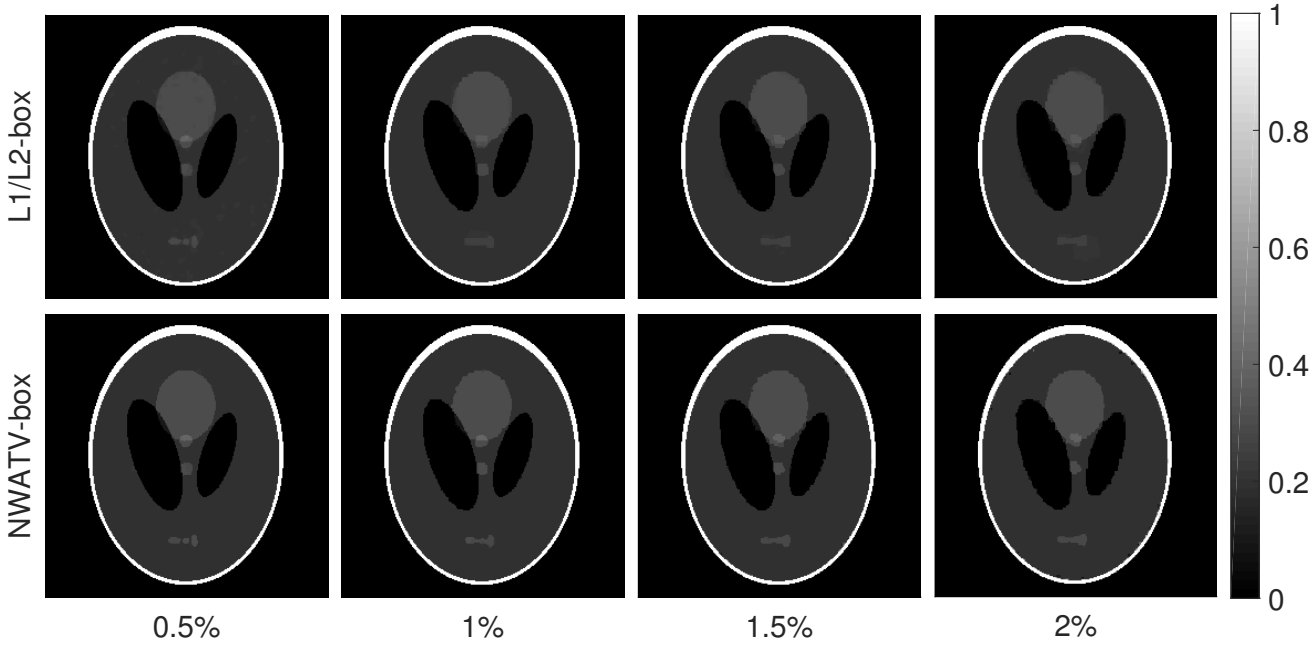

Figure 5. Reconstruction results using the box-constrained NWATV and the box-constrained L_1/L_2 methods with the sampling size 362×90. The top row is the results of the box-constrained L_1/L_2, while the bottom row is the results of the box-constrained NWATV. From left to right are respectively the reconstructed results with noise levels of 0.5%, 1%, 1.5% and 2%.

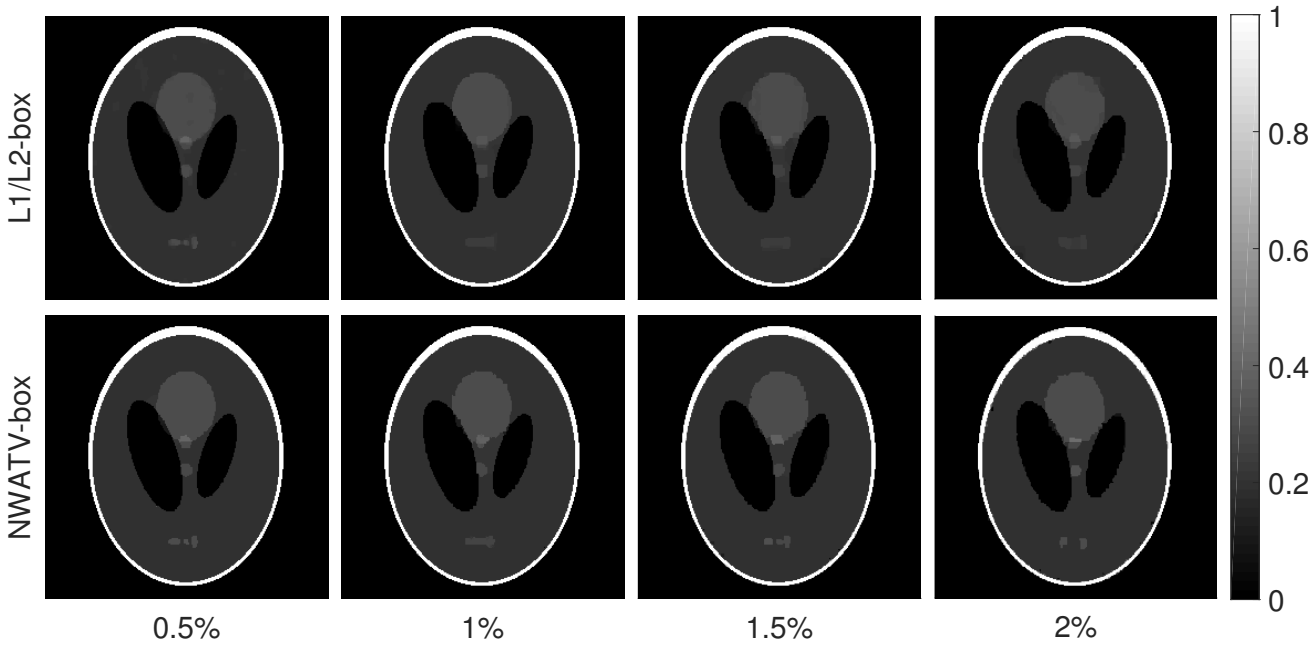

Figure 6. Reconstruction results using box-constrained NWATV and box-constrained L_1/L_2 methods with the sampling size 362×60. Each figure has the similar meaning as that in Figure 5.

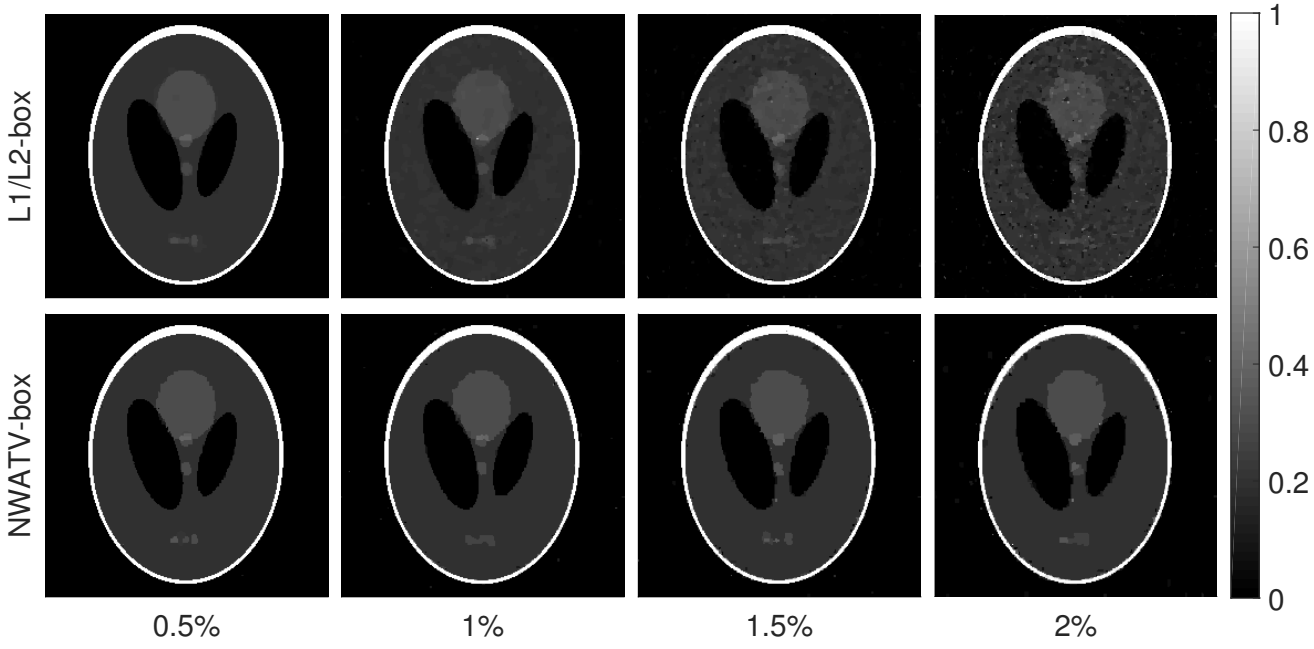

Figure 7. Reconstruction results using the box-constrained NWATV and the box-constrained L_1/L_2 methods with the sampling size 362×30. Each figure has the similar meaning as that in Figure 5.

Table 3. Performance of the box-constrained L_1/L_2 and the box-constrained NWATV regularization for Shepp-Logan phantom for different sampling sizes and noise levels.

	sampling size	noise level (%)	RE	$\widetilde{\text{RE}}$	MSE	PSNR	SSIM	CPU time (s)
L_1/L_2-box	362×90	0.5	0.014	0.025	1.2103×10^{-5}	49.171	0.995	5284.530
		1	0.029	0.051	4.9298×10^{-5}	43.072	0.991	8825.227
		1.5	0.035	0.064	7.5924×10^{-5}	41.196	0.987	5238.058
		2	0.054	0.099	1.7666×10^{-4}	37.530	0.982	5544.499
	362×60	0.5	0.016	0.029	1.4968×10^{-5}	48.248	0.995	1383.701
		1	0.041	0.073	1.0374×10^{-4}	39.841	0.987	5755.229
		1.5	0.072	0.136	3.1424×10^{-4}	35.031	0.983	5202.258
		2	0.090	0.169	4.8614×10^{-4}	33.143	0.980	7313.060
	362×30	0.5	0.022	0.040	2.8187×10^{-5}	45.500	0.993	2419.169
		1	0.049	0.085	1.4510×10^{-4}	38.384	0.968	2537.593
		1.5	0.090	0.156	4.9035×10^{-5}	33.100	0.924	4705.849
		2	0.144	0.247	0.0013	29.013	0.861	2627.596
NWATV-box	362×90	0.5	0.018	0.034	1.8941×10^{-5}	47.229	0.996	239.414
		1	0.035	0.066	7.5532×10^{-5}	41.222	0.991	172.661
		1.5	0.052	0.099	1.6508×10^{-4}	37.829	0.988	150.948
		2	0.073	0.138	3.2454×10^{-4}	34.909	0.982	134.970
	362×60	0.5	0.024	0.045	3.4026×10^{-5}	44.728	0.994	161.004
		1	0.042	0.077	1.0837×10^{-4}	39.651	0.988	148.216
		1.5	0.068	0.129	2.7866×10^{-4}	35.575	0.984	130.353
		2	0.088	0.166	4.6514×10^{-4}	33.344	0.979	140.322
	362×30	0.5	0.039	0.071	9.1074×10^{-5}	40.415	0.989	91.777
		1	0.073	0.136	3.1929×10^{-4}	34.982	0.979	136.941
		1.5	0.105	0.196	6.6875×10^{-4}	31.783	0.968	125.862
		2	0.134	0.248	0.0011	29.658	0.956	137.372

behaves better in edges and details preserving.

In conclusion, through the aforementioned experiments, the box-constrained NWATV method can produce similar and visually better results than the recently developed box-constrained L_1/L_2 method, while the CPU time is significantly decreased.

5. Discussion

Sparse-view CT and limited angle CT are two important ways to reduce the risk of radiation exposure in medical CT scanning. The recent development of artificial intelligence promotes the medical applications of low dose CT [33]. However, recent research has reported the instabilities of such methods [11, 34]. Moreover, to gather the high quality training data, the conventional regularization-based reconstruction methods are still quite necessary. This is because to get the labeled data, without using an elegant regularization, data obtained from the full projections should be

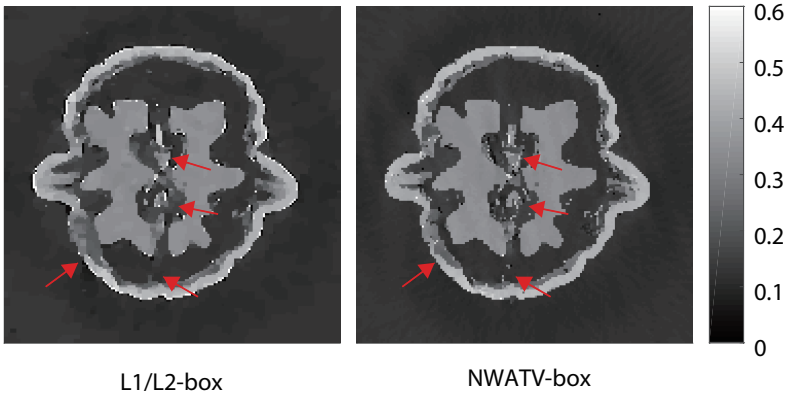

Figure 8. CT reconstruction of walnut. The image size is 164 × 164 and the grayscale window is [0,0.6]. Left: Reconstruction of L_1/L_2-box. Right: Reconstruction of NWATV-box.

Table 4. Comparisons of the performances of two box-constrained methods using the walnut data.

	RE	$\widetilde{\text{RE}}$	MSE	PSNR	SSIM	CPU time (s)
L_1/L_2-box	0.174	0.352	0.0013	24.532	0.804	1568.026
NWATV-box	0.158	0.317	0.0010	25.388	0.798	50.191

employed, which exposes the patient under high risk of radiation.

Another possible model-based approach is the sinogram inpainting method [35]. However, it will cause other artifacts. Hence, proper regularization in the image reconstruction process is a mild way to produce high performance CT images for diagnoses and to gather the training data for AI methodology. [36, 37] provide other ways of combining the model-based and data-driven methods for CT image reconstructions.

5.1. Parameter selection rules

In regularization-based reconstructions, the choice of the regularization parameter is generally very difficult and criticized. However, from the point view of dimensional reduction, we can produce a high performance CT image with a much higher dimension given a small amount of parameters. On the one

Table 5. Comparisons of the performances of two box-constrained methods using the human lung image.

sampling size	model	RE	$\widetilde{\text{RE}}$	MSE	PSNR	SSIM	CPU time (s)
181×60	L_1/L_2-box	0.087	0.177	1.1176×10^{-6}	35.447	0.999	4727.193
	NWATV-box	0.048	0.107	3.4485×10^{-7}	40.635	0.9995	182.108
181×30	L_1/L_2-box	0.120	0.219	2.1427×10^{-6}	32.589	0.997	2592.474
	NWATV-box	0.097	0.195	1.4111×10^{-6}	34.419	0.998	146.728

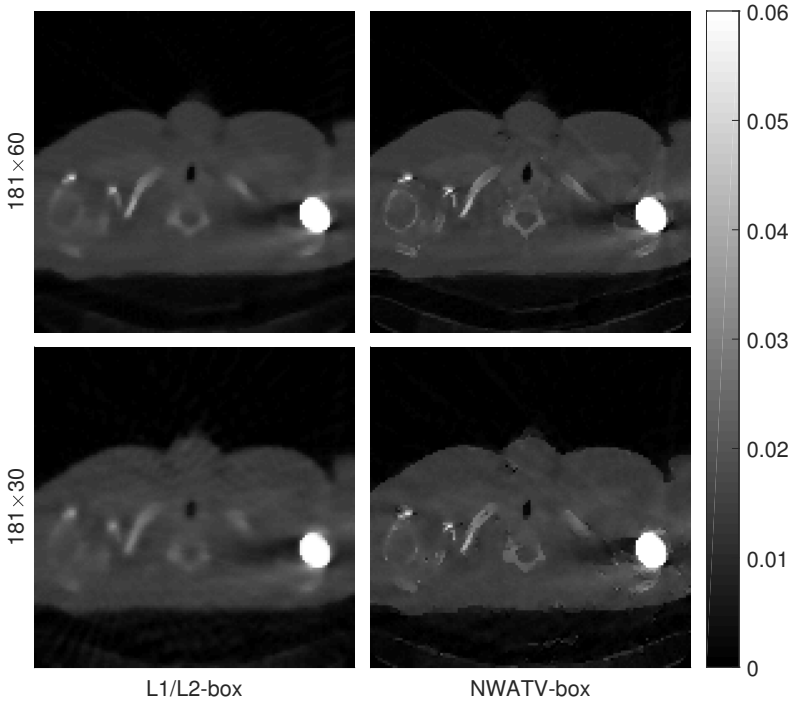

Figure 9. Reconstruction results of the human lung image. The first row depicts the reconstructed images using the box-constrained L_1/L_2 (left) and box-constrained NWATV (right) methods, respectively for the sampling size of 181×60. The second row illustrates the similar results for sampling size of 181×30.

hand, for the choices of the parameters, mathematically there are the discrepancy principle methods and the statistical methods [38] to deal with proper choices of the parameters. On the other hand, there are some rules for the parameters, which are listed as follows.

- As in [24], the performance of the reconstruction (i.e., the relative error depends only the $\frac{\lambda}{\rho}$ rather than the values of λ and ρ).
- The values of ρ and α should be determined by order of A^TA and the number of pixels in such a way that $A^TA + \rho\mathcal{D}^T\mathcal{D} + \alpha\mathcal{I}$ should not change its order.
- The optimal $\frac{\lambda}{\rho}$ value ranges from 10^{-5} to 10^{-4}, since we can minimize the relative error by using such a value.
- The optimal range of λ is approximately 10^{-3} to 10^{-2}.

In Figure 11, we depict the evolution of RE with $\frac{\lambda}{\rho}$ and α for different ρ. From the figures, we can see that for each ρ, RE is invariant with the changes of α when $\frac{\lambda}{\rho}$ is fixed.

5.2. Comparisons on the computation cost with L_1/L_2 method

In this section, we explain the computation load of the proposed box-constrained NWATV method and compare with that in box-constrained L_1/L_2 method [23]. To guarantee the convergence of the box-constrained L_1/L_2 method, both inner and outer loops have to be used, while in the proposed NWATV method, a single loop could produce a good performance of the convergence. Note that in each loop,

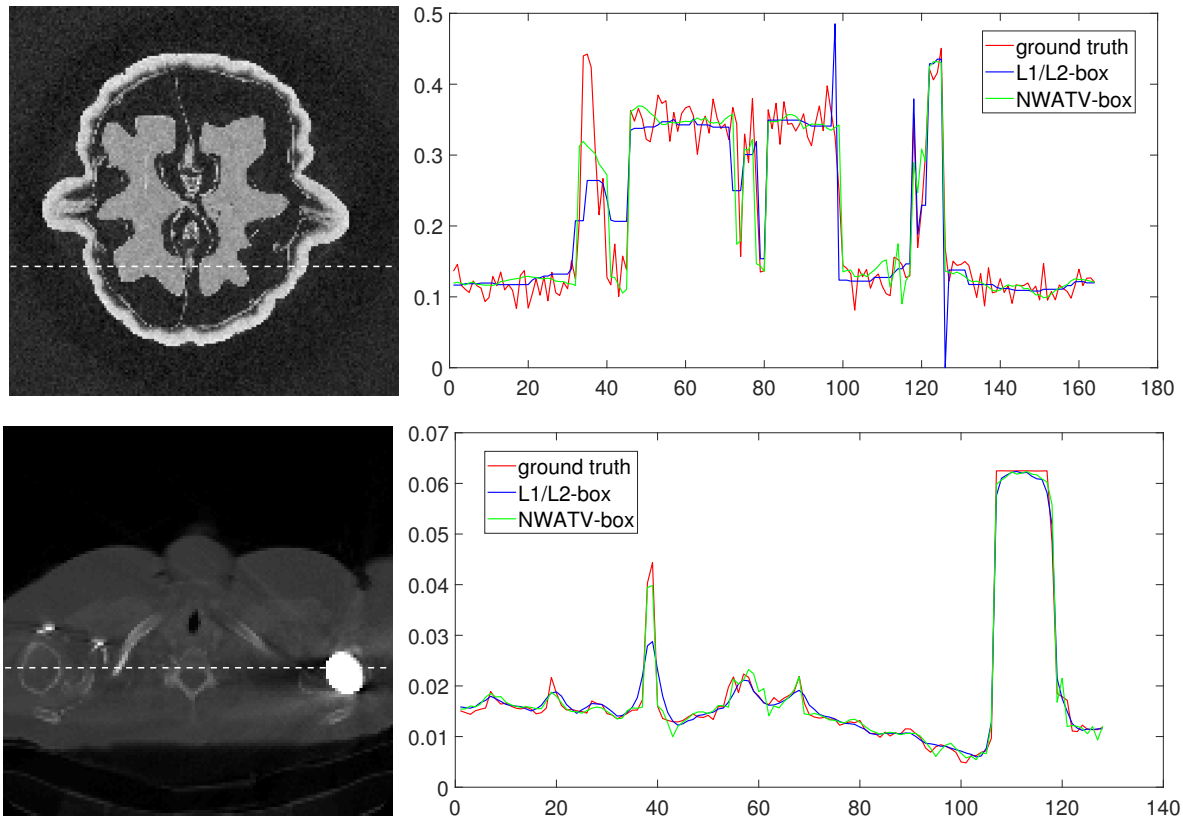

Figure 10. The profiles of the reconstructed walnut and human lung images along the dash lines on left figures. In the right figures, the red line illustrate the values of $\mathbf{u}_0$ along the dash line, the blue line show the values of reconstructions using box-constrained L_1/L_2 methods while the green line depict the reconstructions using box-constrained NWATV methods along the dash lines. The sampling size of the human lung imaging is set to be 181×30.

the most expensive computation is the calculation in (3.6). Similar to [23], in this paper, the maximum number of inner loops is set to be 5, which means that for the same outer loops, the computational load is at least 5 times bigger than that in the proposed method.

6. Conclusions and future works

In this paper, we proposed a box-constrained nonlinear weighted anisotropic TV regularization method and used it in sparse-view CT. Using the Shepp-Logan phantom and the actual walnut models, we validated that the proposed regularization could reconstruct a more accurate CT image than the most recently developed L_1/L_2 regularization method. To be precise, the reconstruction time was reduced more than 8 times while maintaining similar relative errors and a structural similarity index. The proposed method showed advantages, especially when the sampling angles were less than 60 and the noise level was more than 1%. Additionally, numerical simulations displayed a good convergence performance of the proposed iterative scheme. Moreover, since the pixel values of digital images were mostly limited to a certain range, it was reasonable to add box constraints in image processing [1, 23].

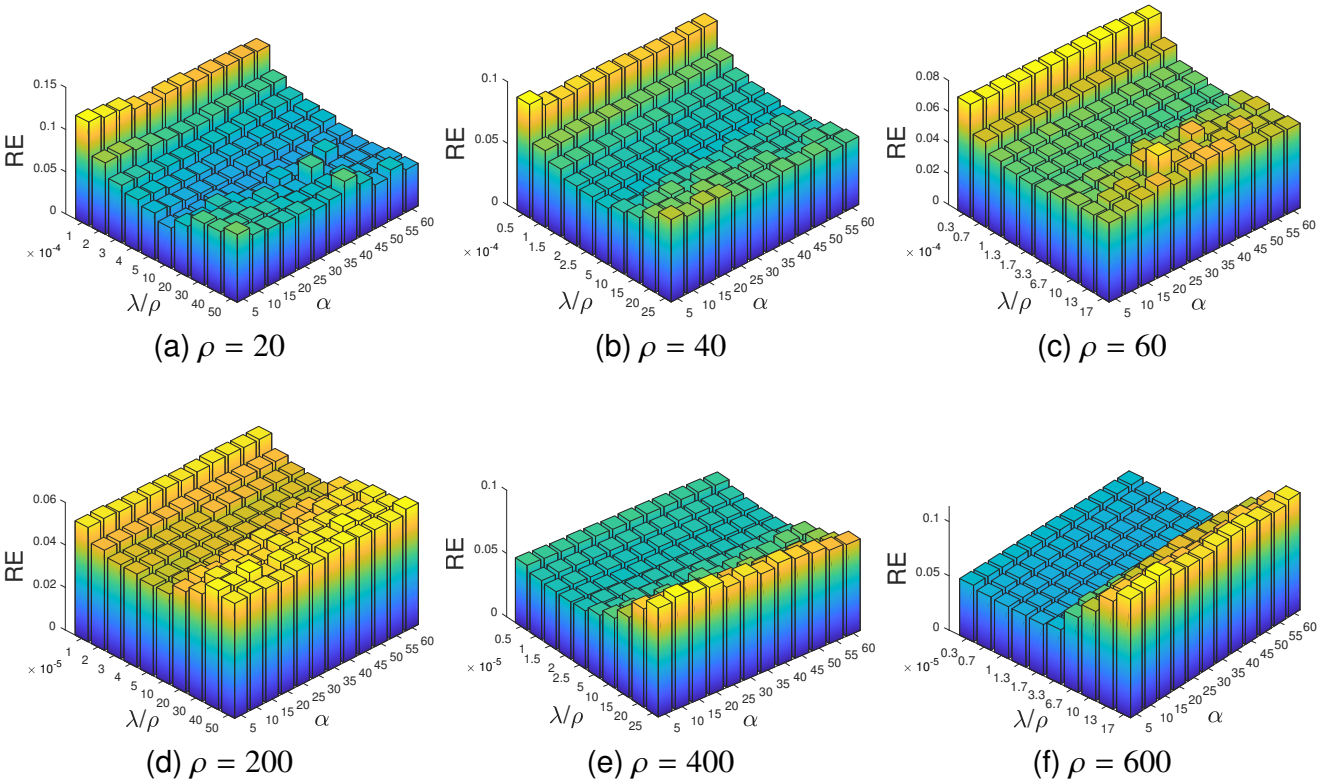

Figure 11. Asymptotic behavior of RE with $\frac{\lambda}{\rho}$ and α. The range of λ is $\{0.002, 0.004, 0.006, 0.008, 0.01, 0.02, 0.04, 0.06, 0.08, 0.1\}$.

Note that errors/noises in the iteration based numerical scheme may accumulate with the iterations, and the box constraint plays the role in suppressing the accumulation in some extent. Hence, the box constraint could enforce the iteration converges to the critical point of the functional $\mathcal{L}$, as shown in Figure 4. We note that in the box-constrained L_1/L_2 method, the authors also note the similar role of the box constraint [23].

Future works should definitely include the mathematical theory of the convergence of the proposed iterative scheme. Moreover, in this paper, we list some rules for the selection of parameters λ, ρ, and α through manual tuning. In the future, we could develop an automatic way to select the optimal parameters by minimizing the discrepancy function in an admissible set using the combinatorial optimization method. If the noise level δ is known, the discrepancy function could be defined as $F(\lambda, \rho, \alpha) = |\|A\mathbf{u}^{\lambda,\rho,\alpha} - \mathbf{y}\| - \tau\delta|$ for a given $\tau > 1$ to avoid underregularization. On the other hand, if the noise level is not known, the Hanke Raus function $F(\lambda, \rho, \alpha) = \|A\mathbf{u}^{\lambda,\rho,\alpha} - \mathbf{y}\|/\lambda$ could be used [39]. To minimize the above functions, we first need to select a good initial guess $\lambda_0, \rho_0, \alpha_0$, and the optimal parameters could be obtained by minimizing the discrepancy functional using an alternate direction iteration scheme. Furthermore, the proposed method can be further used in the area of metal artifact reduction (MAR) in CT reconstruction [40], beam-hardening artifact reduction [41], limited angle artifact reduction [1], and so on.

Use of AI tools declaration

The authors declare they have not used Artificial Intelligence (AI) tools in the creation of this article.

Acknowledgments

This work was supported by Shandong Provincial Outstanding Youth Fund (Grand No. ZR2018JL002), National Natural Science Foundation of China (Grand No. 12271312).

Conflict of interest

The authors declare there is no conflict of interest.

References

1. P. C. Hansen, J. S. Jørgensen, W. R. B. Lionheart, *Computed Tomography: Algorithms, Insight, and Just Enough Theory*, Society for Industrial and Applied Mathematics, Philadelphia, PA, 2021. https://doi.org/10.1137/1.9781611976670
2. F. Natterer, *The Mathematics of Computerized Tomography*, Society for Industrial and Applied Mathematics, Philadelphia, PA, 2001. https://doi.org/10.1137/1.9780898719284
3. C. M. Hyun, T. Bayaraa, S. M. Lee, H. Jung, J. K. Seo, Deep learning for dental cone-beam computed tomography, in *Deep Learning and Medical Applications* (eds. J.K. Seo), Springer Nature Singapore, (2023), 101–175. https://doi.org/10.1007/978-981-99-1839-3_3
4. A. C. Kak, M. Slaney, *Principles of Computerized Tomographic Imaging*, Society for Industrial and Applied Mathematics, Philadelphia, PA, 2001. https://doi.org/10.1137/1.9780898719277
5. E. J. Hall, D. J. Brenner, Cancer risks from diagnostic radiology, *Brit. J. Radiol.*, **81** (2008), 362–378. https://doi.org/10.1259/bjr/01948454
6. M. Chen, Y. F. Pu, Y. C. Bai, Low-dose CT image denoising using residual convolutional network with fractional TV loss, *Neurocomputing*, **452** (2021), 510–520. https://doi.org/10.1016/j.neucom.2020.10.004
7. Z. Hu, D. Liang, D. Xia, H. Zheng, Compressive sampling in computed tomography: method and application, *Nucl. Instrum. Meth. A.*, **748** (2014), 26–32. https://doi.org/10.1016/j.nima.2014.02.026
8. K. H. Jin, M. T. McCann, E. Froustey, M. Unser, Deep convolutional neural network for inverse problems in imaging, *IEEE. T. Image. Process.*, **26** (2017), 4509–4522. https://doi.org/10.1109/TIP.2017.2713099
9. Y. Han, J. C. Ye, Framing U-Net via deep convolutional framelets: Application to sparse-view CT, *IEEE Trans. Med. Imag.*, **37** (2018), 1418–1429. https://doi.org/10.1109/TMI.2018.2823768
10. S. Xie, X. Zheng, Y. Chen, L. Xie, J. Liu, Y. Zhang, et al., Artifact removal using improved GoogLeNet for sparse-view CT reconstruction, *Sci. Rep.*, **8** (2018), 1–9. https://doi.org/10.1038/s41598-018-25153-w

11. E. Y. Sidky, I. Lorente, J. G. Brankov, X. Pan, Do CNNs solve the CT inverse problem?, *IEEE Trans. Biomed. Eng.*, **68** (2021), 1799–1810. https://doi.org/10.1109/TBME.2020.3020741
12. A. Faridani, Introduction to the mathematics of computed tomography, in *Inside Out: Inverse Problems and Applications*, Cambridge Univ. Press, (2003), 1–46. https://doi.org/10.4171/PRIMS/47.1.1
13. S. J. LaRoque, E. Y. Sidky, X. Pan, Accurate image reconstruction from few-view and limited-angle data in diffraction tomography, *J. Opt. Soc. Am. A*, **25** (2008), 1772–1782. https://doi.org/10.1364/JOSAA.25.001772
14. M. Burger, S. Osher, A guide to the TV zoo, in *Level Set and PDE Based Reconstruction Methods in Imaging* (eds. M.Burger and S.Osher), Springer International Publishing, (2013), 1–70. https://doi.org/10.1007/978-3-319-01712-9_1
15. X. Jin, L. Li, Z. Chen, L. Zhang, Y. Xing, Anisotropic total variation for limited-angle CT reconstruction, in *IEEE Nuclear Science Symposuim & Medical Imaging Conference*, (2010), 2232–2238. https://doi.org/10.1109/NSSMIC.2010.5874180
16. Z. Tian, X. Jia, K. Yuan, T. Pan, S. B. Jiang, Low-dose CT reconstruction via edge-preserving total variation regularization, *Phys. Med. Biol.*, **56** (2011), 5949–5967. https://doi.org/10.1088/0031-9155/56/18/011
17. Y. Liu, J. Ma, Y. Fan, Z. Liang, Adaptive-weighted total variation minimization for sparse data toward low-dose x-ray computed tomography image reconstruction, *Phys. Med. Biol.*, **57** (2012), 7923–7956. https://doi.org/10.1088/0031-9155/57/23/7923
18. Y. Xi, P. Zhou, H. Yu, T. Zhang, L. Zhang, Z. Qiao, et al., Adaptive-weighted high order TV algorithm for sparse-view CT reconstruction, *Med. Phys.*, **50** (2023), 5568–5584. https://doi.org/10.1002/mp.16371
19. Y. Wang, Z. Qi, A new adaptive-weighted total variation sparse-view computed tomography image reconstruction with local improved gradient information, *J. X-Ray Sci. Technol.*, **26** (2018), 957–975. https://doi.org/10.3233/XST-180412
20. S. Niu, Y. Gao, Z. Bian, J. Huang, W. Chen, G. Yu, et al., Sparse-view X-ray CT reconstruction via total generalized variation regularization, *Phys. Med. Biol.*, **59** (2014), 2997–3017. https://doi.org/10.1088/0031-9155/59/12/2997
21. Z. Qu, X. Zhao, J. Pan, P. Chen, Sparse-view CT reconstruction based on gradient directional total variation, *Meas. Sci. Technol.*, **30** (2019), 1–11. https://doi.org/10.1088/1361-6501/ab09c6
22. L. Zhang, H. Zhao, W. Ma, J. Jiang, L. Zhang, J. Li, et al., Resolution and noise performance of sparse view X-ray CT reconstruction via Lp-norm regularization, *Phys. Medica.*, **52** (2018), 72–80. https://doi.org/10.1016/j.ejmp.2018.04.396
23. C. Wang, M. Tao, J. Nagy, Y. Lou, Limited-angle CT reconstruction via the L_1/L_2 minimization, *SIAM J. Imaging. Sci.*, **14** (2021), 749–777. https://doi.org/10.1137/20M1341490
24. Y. Song, Y. Wang, D. Liu, A nonlinear weighted anisotropic total variation regularization for electrical impedance tomography, *IEEE Trans. Instrum. Meas.*, **71** (2022), 1–13. https://doi.org/10.1109/TIM.2022.3220288

25. J. Radon, On the determination of functions from their integral values along certain manifolds, *IEEE Trans. Med. Imag.*, **5** (1986), 170–176. https://doi.org/10.1109/TMI.1986.4307775
26. S. Boyd, N. Parikh, E. Chu, B. Peleato, J. Eckstein, Distributed optimization and statistical learning via the alternating direction method of multipliers, *Found. Trends. Mach. Learn.*, **3** (2011), 1–122. https://doi.org/10.1561/2200000016
27. I. Daubechies, M. Defrise, C. De Mol, An iterative thresholding algorithm for linear inverse problems with a sparsity constraint, *Commun. Pur. Appl. Math.*, **57** (2004), 1413–1457. https://doi.org/10.1002/cpa.20042
28. Z. Wang, A. C. Bovik, H. R. Sheikh, E. P. Simoncelli, Image quality assessment: From error visibility to structural similarity, *IEEE. T. Image. Process.*, **13** (2004), 600–612. https://doi.org/10.1109/TIP.2003.819861
29. Y. Saad, M. H. Schultz, GMRES: A generalized minimal residual algorithm for solving nonsymmetric linear systems, *SIAM J. Sci. Stat. Comput.*, **7** (1986), 856–869. https://doi.org/10.1137/0907058
30. P. C. Hansen, J. S. Jørgensen, AIR Tools II: Algebraic iterative reconstruction methods, improved implementation, *Numer. Algor.*, **79** (2018), 107–137. https://doi.org/10.1007/s11075-017-0430-x
31. K. Hämäläinen, L. Harhanen, A. Kallonen, A. Kujanpää, E. Niemi, S. Siltanen, Tomographic X-ray data of a walnut, preprint, arXiv:1502.04064. https://doi.org/10.48550/arXiv.1502.04064
32. O. Grove, A. E. Berglund, M. B. Schabath, H. J. W. L. Aerts, A. Dekker, H. Wang, et al., Quantitative computed tomographic descriptors associate tumor shape complexity and intratumor heterogeneity with prognosis in lung adenocarcinoma, *PLoS ONE*, **10** (2015), 1–14. https://doi.org/10.1371/journal.pone.0118261
33. G. Wang, J. C. Ye, B. D. Man, Deep learning for tomographic image reconstruction, *Nat. Mach. Intell.*, **2** (2020), 737–748. https://doi.org/10.1038/s42256-020-00273-z
34. V. Antun, F. Renna, C. Poon, B. Adcock, A. C. Hansen, On instabilities of deep learning in image reconstruction and the potential costs of AI, *P. Natl. A. Sci.*, **117** (2020), 30088–30095. https://doi.org/10.1073/pnas.1907377117
35. S. Li, Q. Cao, Y. Chen, Y. Hu, L. Luo, C. Toumoulin, Dictionary learning based sinogram inpainting for CT sparse reconstruction, *Optik*, **125** (2014), 2862–2867. https://doi.org/10.1016/j.ijleo.2014.01.003
36. E. Kobler, A. Effland, K. Kunisch, T. Pock, Total deep variation: A stable regularization method for inverse problems, *IEEE. T. Pattern. Anal.*, **44** (2022), 9163–9180. https://doi.org/10.1109/TPAMI.2021.3124086
37. J. Xu, F. Noo, Convex optimization algorithms in medical image reconstruction—in the age of AI, *Phys. Med. Biol.*, **67** (2022), 1–77. https://doi.org/10.1088/1361-6560/ac3842
38. J. Kaipio, E. Somersalo, *Statistical and Computational Inverse Problems*, Springer, New York, 2005. https://doi.org/10.1007/b138659
39. L. Xu, L. Li, W. Wang, Y. Gao, CT image reconstruction algorithms based on the Hanke Raus parameter choice rule, *Inverse Probl. Sci. Eng.*, **28** (2020), 87–103. https://doi.org/10.1080/17415977.2019.1628739

40. H. Park, J. K. Choi, J. K. Seo, Characterization of metal artifacts in X-ray computed tomography, *Commun. Pure Appl. Math.*, **70** (2017), 2191–2217. https://doi.org/10.1002/cpa.21680

41. S. M. Lee, J. K. Seo, Y. E. Chung, J. Baek, H. S. Park, Technical Note: A model-based sinogram correction for beam hardening artifact reduction in CT, *Med. Phys.*, **44** (2017), e147–e152. https://doi.org/10.1002/mp.12218

AIMS Press